Quantum Electronics **52** (6) 505–512 (2022)

https://doi.org/10.1070/QEL18062

Effect of optical lattice field on characteristics of a clock transition in thulium atoms

D.A. Mishin, D.I. Provorchenko, D.O. Tregubov, A.A. Golovizin, K.Yu. Khabarova, V.N. Sorokin, N.N. Kolachevsky

Abstract. **This paper presents a detailed analysis of the effect of the optical lattice field on clock transition spectroscopy, as exemplified by thulium atoms. We consider the applicability of the sifting of atoms in an optical lattice by ramping down the power of the laser light that produces it. This method allows the number of filled vibrational sublevels to be reduced down to a single vibrational state, without changing the inner state of the atoms. The effectiveness of the method is illustrated by the example of the spectroscopy of a clock transition in thulium atoms in the resolved sideband regime.**

Keywords: *spectroscopy, optical clock, laser cooling, optical lattice, ultracold atoms, thulium.*

1. Introduction

The transition of frequency standards to the optical range allowed a relative uncertainty and instability at a level of 10^{-18} to be reached [1]. At present, optical frequency standards based on Al^+ [2], Yb^+ [3], and neutral strontium atoms [4] are the most accurate. Clocks based on neutral atoms in optical lattices demonstrate considerably better stability than do single-ion clocks. All types of optical clocks require deep cooling of particles, and Doppler and sub-Doppler laser cooling methods allow temperatures of the order of a few microkelvins to be reached [5]. The next step in all state-of-the-art optical clocks is the transition to the so-called Lamb–Dicke regime, which allows the contributions of the linear Doppler and recoil effects to be suppressed [6]. To pass into this regime, it is necessary to localise atoms in the propagation direction of probe light on a length scale smaller than its wavelength. In optical clocks based on neutral atoms, magic-wavelength optical lattices are used for this purpose [7–10], in order to reduce the effect of the confining potential on the clock transition frequency. This method leads in a natural way to discrete energy levels corresponding to vibrational states in the optical lattice potential. The distribution of atoms over vibrational states can result in a number of effects undesirable in the case of precision spectroscopy. These include, for example, Rabi oscillation decoherence [11] and the dependence of the clock transition frequency shift on the vibrational state, due to higher order polarisabilities [12]. Such problems are encountered in dealing with various atomic standards and can be solved most frequently by pumping atoms into the vibrational ground state using sideband cooling [12, 13]. For thulium atoms, this approach can be implemented using one of their narrow transitions, e.g., that considered by Provorchenko et al. [14]. However, it leads to a magnetic sublevel population redistribution. This is critical in the case of thulium atoms because clock transition spectroscopy is performed between states with a total momentum projection $m_F = 0$ [15, 16].

In this paper, we analyse the above-mentioned Rabi oscillation decoherence and clock transition frequency shift effects, related to the distribution of atoms over vibrational sublevels. In addition, we analyse whether sifting of atoms via a temporary reduction in optical lattice depth can be used in thulium optical clocks. This method allows the number of filled vibrational sublevels to be reduced without changes in inner states of the atoms [15–19].

2. Interaction of atoms with an optical lattice and the vibrational spectrum of the transitions

In this section, interaction of atoms with monochromatic light is described in terms of polarisabilities. In the dipole approximation, the energy shift of the ith level can be written in the form

$$\Delta E_i(\boldsymbol{r},\omega) = -\frac{1}{4}(4\pi\varepsilon_0 a_0^3)\alpha_i(\omega)E_0^2(\boldsymbol{r})$$

$$= -\alpha_i(\omega)\frac{2\pi a_0^3}{c}I(\boldsymbol{r}), \qquad (1)$$

where $\alpha_i(\omega)$ is the dynamic polarisability of the level, expressed in atomic units, at the corresponding frequency; ε_0, a_0, and c are the permittivity of vacuum, the Bohr radius, and the speed of light in vacuum, respectively; and $E_0(\boldsymbol{r})$ and $I(\boldsymbol{r}) = (c\varepsilon_0/2)|E_0(\boldsymbol{r})|^2$ are the amplitude and intensity of light at the point under consideration. Thus, the spatial intensity distribution determines a potential that confines atoms under certain conditions.

Hereafter, we consider a Gaussian TEM_{00} mode and standing-wave configuration. It is convenient to represent this configuration as a combination of two counterpropagating beams, which are thought to have equal powers in subse-

D.A. Mishin, K.Yu. Khabarova, N.N. Kolachevsky P.N. Lebedev Physical Institute, Russian Academy of Sciences, Leninsky prosp. 53, 119991 Moscow, Russia; International Center for Quantum Technologies, Bol'shoi blv. 30/1, Skolkovo Innovation Center Area, 121205 Moscow, Russia; e-mail: mishin.da@phystech.edu;
D.I. Provorchenko, D.O. Tregubov, A.A. Golovizin, V.N. Sorokin P.N. Lebedev Physical Institute, Russian Academy of Sciences, Leninsky prosp. 53, 119991 Moscow, Russia

Received 22 March 2022; revision received 29 April 2022
Kvantovaya Elektronika **52** (6) 505–512 (2022)
Translated by O.M. Tsarev

quent formulas. The depth of the potential for the ith level can be represented as

$$U(\boldsymbol{r}) = -4\frac{2\pi a_0^3}{c}\alpha_i I_\mathrm{p}(\boldsymbol{r}),$$

where α_i is the polarisability of the level under consideration and $I_\mathrm{p}(\boldsymbol{r})$ is the intensity of the wave propagating in the forward direction. Near the beam waist, relation (1) can be written through the maximum depth of the potential,

$$U_0 = \frac{8\pi a_0^3}{c}\alpha_i I_0,$$

expressed through the maximum intensity on the beam axis,

$$I_0 = \frac{2P}{\pi w^2}$$

(here, w is the $1/e^2$ Gaussian beam radius and P is the power of the wave propagating in the forward direction):

$$U(r,z) = -U_0\,\mathrm{e}^{-2r^2/w^2}\cos^2(k_\mathrm{lat}z), \tag{2}$$

where $k_\mathrm{lat} = 2\pi/\lambda_\mathrm{lat} = 2\pi\nu_\mathrm{lat}/c$ is the magnitude of the wave vector of the light that produces the optical lattice along the Z axis; r is the distance from the lattice axis; and z is the distance from the beam waist. Hereafter, we consider the potential of an individual standing wave cell with the z coordinate measured from the antinode position. At small distances r from the lattice axis, the potential can be approximated by a harmonic one,

$$\begin{aligned} U^\mathrm{h}(z,r) &= -U_0 + \frac{m}{2}\omega_r^2 r^2 + \frac{m}{2}\omega_z^2 z^2 \\ &= U_0\left(-1 + k_\mathrm{lat}^2 z^2 + 2\frac{r^2}{w_0^2}\right), \end{aligned} \tag{3}$$

with transverse and longitudinal vibration frequencies

$$\omega_r = \frac{8}{w_0^2}\sqrt{\frac{a_0^3\alpha_\mathrm{g}P}{cm}} = 2\sqrt{\frac{U_0}{mw_0^2}}$$

and

$$\omega_z = \frac{\sqrt{2}\,\pi w_0}{\lambda_\mathrm{lat}}\omega_r = 2\times 2\pi\nu_\mathrm{rec}\sqrt{\frac{U_0}{E_\mathrm{rec}}},$$

respectively, where $E_\mathrm{rec} = (h\nu_\mathrm{lat}/c)^2/2m$ and $\nu_\mathrm{rec} = E_\mathrm{rec}/h$ are the recoil energy and frequency related to scattering of optical lattice photons; α_g is ground state polarisability; w_0 is the beam waist radius; and m is the particle mass. The characteristic number of vibrational levels in the approximation under consideration can be estimated as follows:

$$\begin{aligned} N_z &\approx U_0/\hbar\omega_z = \sqrt{\frac{U_0}{4E_\mathrm{rec}}}, \\ N_r &\approx N_z\frac{\nu_z}{\nu_r}. \end{aligned} \tag{4}$$

Here, we use the designations $\nu_r = \omega_r/2\pi$ and $\nu_z = \omega_z/2\pi$. Taking into account further corrections in the expansion of (2) yields the following relations for the lattice potential and energy spectrum:

$$U(z,r) = U_0\left(-1 + k_\mathrm{lat}^2 z^2 + 2\frac{r^2}{w_0^2} - \frac{k_\mathrm{lat}^4 z^4}{3} - 2\frac{k_\mathrm{lat}^2}{w_0^2}z^2 r^2\right), \tag{5}$$

$$\begin{aligned} E_{n_z n_r}/h \cong\ & \nu_z\left(n_z + \frac{1}{2}\right) + \nu_r\left(n_r + \frac{1}{2}\right) - \frac{\nu_\mathrm{rec}}{2}\left(n_z^2 + n_z + \frac{1}{2}\right) \\ & -\nu_\mathrm{rec}\frac{\nu_r}{\nu_z}\left(n_z + \frac{1}{2}\right)\left(n_r + \frac{1}{2}\right), \end{aligned} \tag{6}$$

where n_z and n_r are the numbers of the longitudinal and radial vibrational levels, respectively. If the last term in (6) is neglected, the energy as a function of n_z can be presented in the form

$$E_{n_z}/h = \nu_z\left(n_z + \frac{1}{2}\right) - \frac{\nu_\mathrm{rec}}{2}\left(n_z^2 + n_z + \frac{1}{2}\right).$$

Note that, if atoms are confined in an optical lattice at the magic wavelength, the potentials for the ground and upper clock levels have the same depth and vibrational spectrum. It is seen from (6) that taking into account the corrections causes the spacing between vibrational levels to decrease with increasing n_z and n_r as

$$(E_{n_z+1} - E_{n_z})/h = \nu_z - \nu_\mathrm{rec}(n_z + 1).$$

This dependence leads to asymmetry of profiles in the case of spectroscopy at sideband frequencies. Fedorova et al. [11] and Blatt et al. [20] obtained probability density as a function of probe light frequency detuning δ for a transition with a change in the longitudinal vibrational quantum number by unity:

$$\begin{aligned} p_{n_z}(\delta) &= \Theta[\tilde{\nu}_{n_z} - |\,\delta\,|]\frac{\chi^2}{\tilde{\nu}_{n_z}}\left(1 - \frac{\delta}{\tilde{\nu}_{n_z}}\right)\exp[-\chi(1 - \delta/\tilde{\nu}_{n_z})], \\ p_{+1(-1)}(\delta) &= \frac{1}{Z(T_z)}\sum_{n_z=0(1)}^{N_z}\exp(-E_{n_z}/k_\mathrm{B}T_z)p_{n_z}(\delta), \\ p_\mathrm{total}(\delta) &= p_{-1}(\delta)\Theta[-\delta] + p_{+1}(\delta)\Theta[\delta]. \end{aligned} \tag{7}$$

Here, p_{n_z} corresponds to the probability of a transition from state n_z to neighbouring vibrational states; $p_{+1(-1)}$ allows the blue (red) wing of the distribution to be described; p_total describes both sidebands;

$$\tilde{\nu}_{n_z} = \nu_z - \nu_\mathrm{rec}(n_z + 1);$$

$$\chi = (\tilde{\nu}_{n_z}/\nu_\mathrm{rec})\frac{h\nu_z}{k_\mathrm{B}T_r};$$

N_z is the total number of bound levels in the lattice potential, which can be found using numerical simulation or estimated

using relations (4); T_r and T_z are the temperatures corresponding to distributions over transverse and longitudinal vibrational modes;

$$Z(T_z) = \sum_{n_z=0}^{N_z} \exp(-E_{n_z}/k_B T_z)$$

is the partition function; and $\Theta[x]$ is the Heaviside function. The cause of the distinction between the blue (+1) and red (–1) vibrational sidebands is that there is no $\Delta n_z = -1$ transition for the ground vibrational sublevel. Sideband frequency spectra contain information about the distribution of atoms over vibrational sublevels and characteristic temperatures of such distributions. The information can be extracted by fitting the spectra to relation (7), with ν_z, T_z, and T_r as fit parameters, and utilised for analysis of a number of effects described below. Figure 1 presents characteristic spectroscopy results and optical lattice parameters evaluated by fitting the spectrum to relation (7).

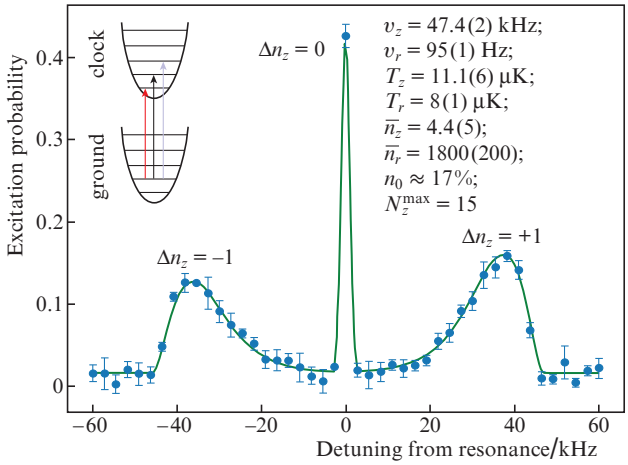

Figure 1. (Colour online) Spectroscopy results for a clock transition in the resolved sideband regime. Fitting the experimental data to relation (7) (solid line) allows parameters of the lattice and characteristics of the atom distribution to be estimated. Also indicated are the longitudinal and transverse vibration frequencies (ν_z and ν_r), estimated temperatures of the distribution over the corresponding vibrational sublevels (T_z and T_r), average values of vibrational states ($\bar{n}_z$ and $\bar{n}_r$), population of the ground longitudinal ($n_z = 0$) vibrational level (n_0), and the total number of vibrational states ($N_z^{\max}$).

3. Clock transition frequency shift

Consider now the frequency shift of a clock transition between the ground and clock states, g → c, due to interaction with the optical lattice. Analysing the electric dipole (E1) mechanism of interaction, one can find so-called magic wavelengths, at which the ground and clock states have equal electric dipole polarisabilities, α_i^{E1}. At the magic wavelengths, the frequency shift of the transition under consideration is independent of light intensity and turns out to be zero for atoms in all vibrational states. However, to reach uncertainty and instability at a level of 10^{-18}, it is necessary to take into account corrections to interaction of atoms with light [21]: interaction by magnetic-dipole and electric-quadrupole mechanisms (α_i^{qm}) and hyperpolarisability of atoms (β_i). We then obtain

$$U(I_0,z) = -\left(\frac{2\pi a_0^3}{c}\right)[\alpha_i^{E1} I_0 \cos^2(k_{lat} z) + \alpha_i^{qm} I_0 \sin^2(k_{lat} z)]$$

$$-\frac{\pi^2 m_e a_0^8}{\hbar^2 c^2}\beta_i I_0^2 \cos^4(k_{lat} z), \qquad (8)$$

where m_e is the mass of an electron. The mechanisms under consideration were analysed, e. g., by Ushijima et al. [12] and Beloy et al. [22]. For convenience of subsequent reasoning, we introduce a normalised depth: $u = U_0/E_{rec}$. The radial vibrational frequency being low compared to the lattice depth allows the intensity of light with which atoms interact to be averaged over the transverse vibrational sublevels and the following attenuation coefficients to be introduced,

$$\zeta_j \approx 1 - \frac{j k_B T_r}{u E_{rec}},$$

which relate the powers of the maximum mormalised optical lattice depth to the corresponding powers of some effective depth $\bar{u}^j = \zeta_j(u, T_r)u^j$ for atoms at a particular radial temperature T_r. Here, j is the exponent under consideration in the expansion of potential (8). Since the terms of potential (8) have different spatial dependences, the clock transition frequency shift depends on the longitudinal vibrational state of the atoms, n_z, which can be represented by the relation

$$h\Delta\nu(\delta_{mw}, n_z, \bar{u}) \approx \left(\frac{\partial\tilde{\alpha}^{E1}}{\partial\nu}\delta_{mw} - \tilde{\alpha}^{qm}\right)\left(n_z + \frac{1}{2}\right)\bar{u}^{1/2}$$

$$-\left[\frac{\partial\tilde{\alpha}^{E1}}{\partial\nu}\delta_{mw} + \frac{3}{2}\tilde{\beta}\left(n_z^2 + n_z + \frac{1}{2}\right)\right]\bar{u}$$

$$+ 2\tilde{\beta}\left(n_z + \frac{1}{2}\right)\bar{u}^{3/2} - \tilde{\beta}\bar{u}^2, \qquad (9)$$

where δ_{mw} is the detuning of the frequency of the light that produces the optical lattice from the E1 magic frequency and the following designations of normalised polarisabilities are used:

$$\tilde{\alpha}^{E1} = (\alpha_e^{E1} - \alpha_g^{E1})\frac{E_{rec}}{\alpha_g^{E1}},$$

$$\tilde{\alpha}^{qm} = (\alpha_e^{qm} - \alpha_g^{qm})\frac{E_{rec}}{\alpha_g^{E1}}, \qquad (10)$$

$$\tilde{\beta} = \left(\frac{m_e a_0^2}{4\hbar^2}\right)(\beta_e - \beta_g)\left(\frac{E_{rec}}{\alpha_g^{E1}}\right)^2.$$

One promising magic wavelength for a clock transition in thulium atoms lies near 1064 nm [17]. Given below are a number of parameters essential for evaluating interaction of atoms with light at this wavelength – thulium atom polarisability characteristics [15] and recoil energy corresponding to light of an optical lattice at this wavelength:

E_{rec}/h, Hz 1043
E_{rec}/k_B, nK 50
α_g^{E1} (a.u.) 152
$\partial\tilde{\alpha}^{E1}/(h\partial\nu)$ . . . . . 1.6×10^{-14}
$\tilde{\alpha}^{qm}/h$, mHz 1.2
$\tilde{\beta}/h$, nHz . . . . . –1.5

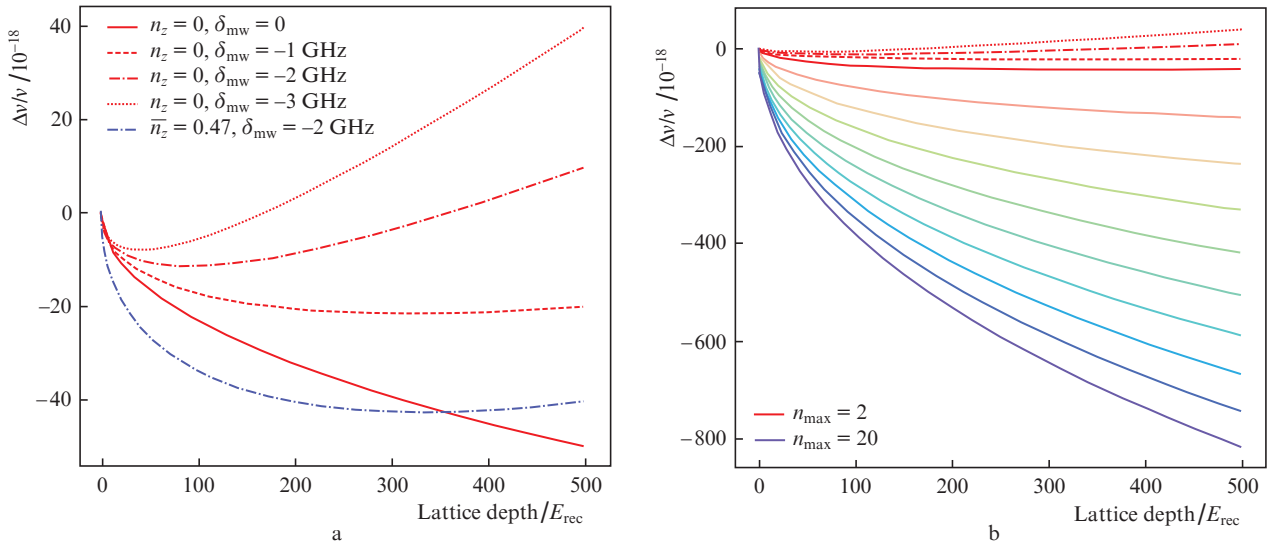

Figure 2. (Colour online) (a) Clock transition frequency (p) shift as a function of optical lattice depth for the vibrational ground level at various detuning values δ_{mw} (red lines) and for atoms distributed over the first two vibrational sublevels according to the characteristics indicated in Fig. 1 (blue dot-dashed line). (b) Frequency shift as a function of lattice depth at various values of the maximum number of occupied levels in the case of 20 accessible levels. The detuning from the E1 magic wavelength is $\delta = -2$ GHz. The red lines in panel b are analogous to those in panel a.

Figure 2 shows the clock transition frequency shift as a function of optical lattice depth at various detuning values. It is seen that the clock transition frequency shift varies from 2×10^{-17} in the case of the first vibrational level occupied (in comparison with atoms in the ground state) to more than 4×10^{-16} (at $u = 100$). The difference in frequency shift is quite appreciable, so it is necessary to accurately characterise and monitor the distribution of atoms over vibrational levels. As shown by Ushijima et al. [12], this effect can be used to determine high-order polarisability coefficients. In Section 5, we consider the method we use to remove atoms from high vibrational levels.

4. Dependence of the Rabi frequency on the vibrational state of atoms

The atom population distribution over vibrational sublevels leads as well to Rabi frequency nonuniformity when a clock light pulse is applied [11, 20]. In the Lamb–Dicke regime with a localisation parameter

$$\eta_z^2 = \nu_{rec}^{clock}/\nu_z,$$

where

$$\nu_{rec}^{clock} = h\nu_{clock}^2/2mc^2$$

is the recoil frequency corresponding to clock light scattering, the Rabi frequency for a transition with no change in the vibrational state depends on the quantum number n_z as

$$\Omega_{n_z} = \Omega_0 \exp(-\eta_z^2/2)\, L_{n_z}(\eta_z^2), \tag{11}$$

where Ω_0 is the Rabi frequency for a free atom and $L_{n_z}(x)$ is a Laguerre polynomial. Here, we neglect the dependence of the Rabi frequency on the radial quantum number because we assume that there is rather good alignment of the probe clock light and the light that produces the optical lattice (better than 10^{-3} rad [10]). The shifts due to higher order polarisabilities are here also left out of account because they are small compared to the Rabi frequency characteristic of our experiment: of the order of 1 kHz. Thus, atoms at each particular vibrational sublevel, n_z, will undergo Rabi oscillations of their upper level population at different frequencies:

$$p_{n_z}^{e}(t) = \sin^2(\Omega_{n_z} t).$$

The experimentally observed total population of the upper level, with allowance for spontaneous decay [23] with an inverse lifetime $\Gamma = 2\pi \times 1.4$ s^{-1} [24, 25] (which is, however, unimportant in our case), can be expressed through sublevel populations $\rho_{n_z} \sim \exp(-E_{n_z}/k_B T_z)$ as

$$p^{e}(t) = \sum_{n_z=0}^{n_z=N_z^{max}} \frac{\rho_{n_z}}{2}\left[1 - \cos(2\Omega_{n_z} t)\exp\left(-\frac{3}{4}t\Gamma\right)\right]. \tag{12}$$

Rabi oscillations typical of thulium atoms after optical pumping are shown in Fig. 3. By fitting to relation (12), we were able to estimate the average population of vibrational levels, $\overline{n_z} = 8.0(0.2)$, and the Lamb–Dicke parameter, $\eta_z = 0.14$. The red dotted line represents Rabi oscillations in the case where only the vibrational ground state is populated. For a more detailed analysis of the atom sifting method proposed below, it is of interest to pay attention to Rabi oscillations at the same average vibrational quantum number $\overline{n_z} = 4.1$ but different population distributions over vibrational levels. The violet dashed line corresponds to a distribution at constant temperature T_z and empty levels with $n \geqslant 10$, and the green dot-dashed line represents the Boltzmann distribution over all accessible vibrational states with reduced $\tilde{T}_z = T_z/4$. It is seen that, in the latter case, oscillations decay considerably

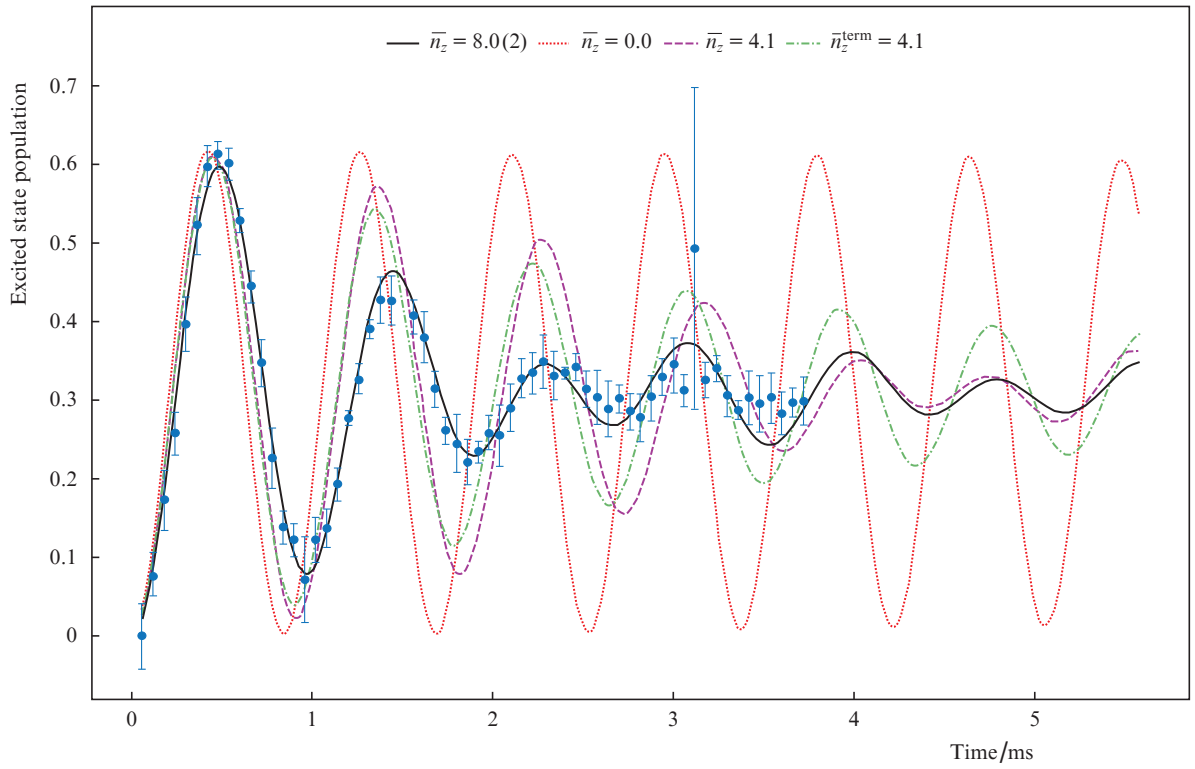

Figure 3. (Colour online) Rabi oscillations. Experimental data (blue filled circles) were fitted by function (12) with the limitation $N_z^{\max} = 20$ (black solid line). Also shown are calculated Rabi oscillations in the case where only the vibrational ground state ($\bar{n}_z = 0$) is populated (red dotted line). The violet dashed line corresponds to an average population $\bar{n}_z = 4.1$ in the case of T_z and empty vibrational levels with $n \geqslant 10$, and the green dot-dashed line corresponds to population of all 20 levels with a temperature $\tilde{T}_z = T_z/4$ and the same average value $\bar{n}_z$.

more slowly. Whereas the curves are essentially identical at short times, the difference between them is appreciable at long times. Therefore, the two cases under consideration can theoretically be distinguished from the shape of Rabi oscillations.

From the viewpoint of operation of an optical clock, the population distribution over a large number of vibrational levels leads to a reduction in the maximum achievable fraction of excited atoms and, as a consequence, a reduction in the slope of the error signal.

5. Sifting of atoms

The laser cooling methods we use imply spontaneous decay to the ground state. After optical pumping to the $m_F = 0$ sublevel, they cannot be used because depolarisation of atoms will occur. However, it is the preparation of initial states which makes the major contribution to heating of atoms. This causes a number of undesirable effects, considered above. To resolve this issue, we propose that the optical lattice potential be temporarily ramped down by reducing the number of

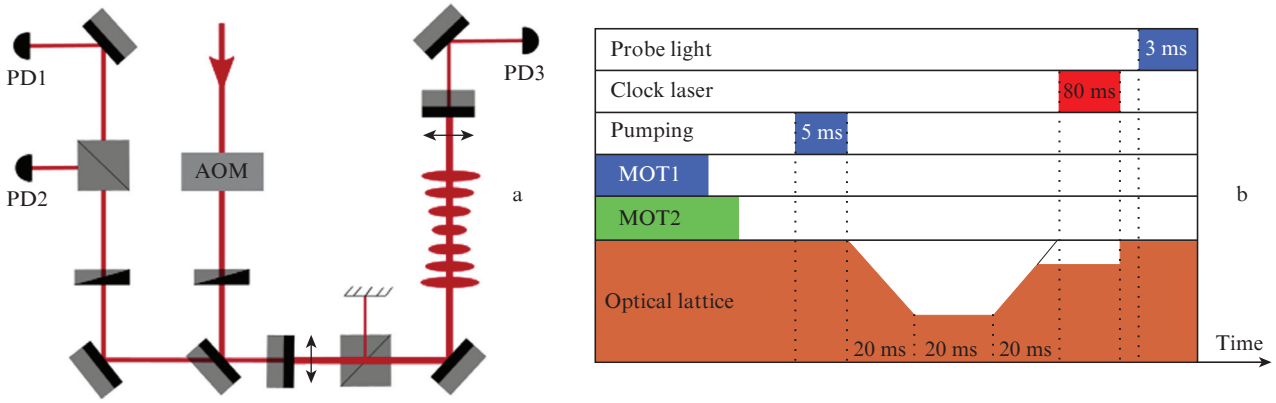

Figure 4. (Colour online) (a) Schematic illustrating the formation of an optical lattice and (b) pulse diagram of the experiment. A fibre laser beam is sent to an acousto-optic modulator (AOM), which allows the power of the light that produces an optical lattice to be varied. The first order diffracted beam is then launched into an enhancement cavity, whose length is stabilised by the Hänsch–Couillaud method using photodiodes PD1 and PD2; PD3 is used to measure the power of the light circulating in the cavity, with allowance for the transmittance of the output coupler.

bound states, which will lead to a reduction in the number of filled vibrational levels during clock transition spectroscopy, without disturbing the distribution of atoms over magnetic sublevels. In experiments, this can be brought about using an acousto-optic modulator to reduce the power of the light that produces the optical lattice (Fig. 4a). Figure 4b shows a characteristic time dependence of this power.

In an experimental setup, a lattice is produced using light from an Azurlight ALS-10W1064 fibre laser at a wavelength of 1064 nm. The light passes through an acousto-optic modulator, and then the first order diffracted beam enters a vacuum chamber. To increase the maximum attainable depth of the potential and improve the efficiency of atom recapture from a magneto-optical trap, an enhancement cavity is used [26]. In addition, it allows one to monitor geometric beam parameters necessary for calculations of intensity, the corresponding depth of the potential, and longitudinal and transverse vibrational frequencies. The cavity length is stabilised to the light wavelength by the Hänsch–Couillaud method, and the TEM_{00} mode waist radius is 120 μm.

In the course of experiments, capture of atoms in the magneto-optical trap, recapture in the optical lattice, and optical pumping are performed at the maximum depth of the potential, approximately $516E_{rec}$, which corresponds to a longitudinal vibrational frequency of 47.4(2) kHz. The maximum concentration of atoms recaptured in the optical lattice at these parameters does not exceed 10^{10} cm^{-3}. The atoms are then held at the quasi-two-dimensional standing wave antinodes, with a characteristic size $\lambda_{lat}/2$. After the above processes, the optical power of the lattice is adiabatically reduced (Fig. 4b). Clock transition spectroscopy is then conducted at some final power necessary in the experiment, and states are read out again at the maximum lattice depth (Fig. 4b).

The experimental setup we use allows for variations in optical lattice power between different clock transition spectroscopy cycles, which makes it possible to study spectra of vibrational sublevels at various atom distributions and also transition frequency shifts induced by interaction with the light of the lattice. The clock transition is excited by a high-power laser pulse at a wavelength of 1.14 μm, following which the populations of various states of atoms are read out as described elsewhere [15], which allows the excitation probability to be calculated. The upper panels in Fig. 5 present measurement results obtained before and after sifting, and the lower panels present simulation results for bound states in the lattice potential.

First of all, attention should be paid to the fact that the maximum excitation probability is the same in all our experi-

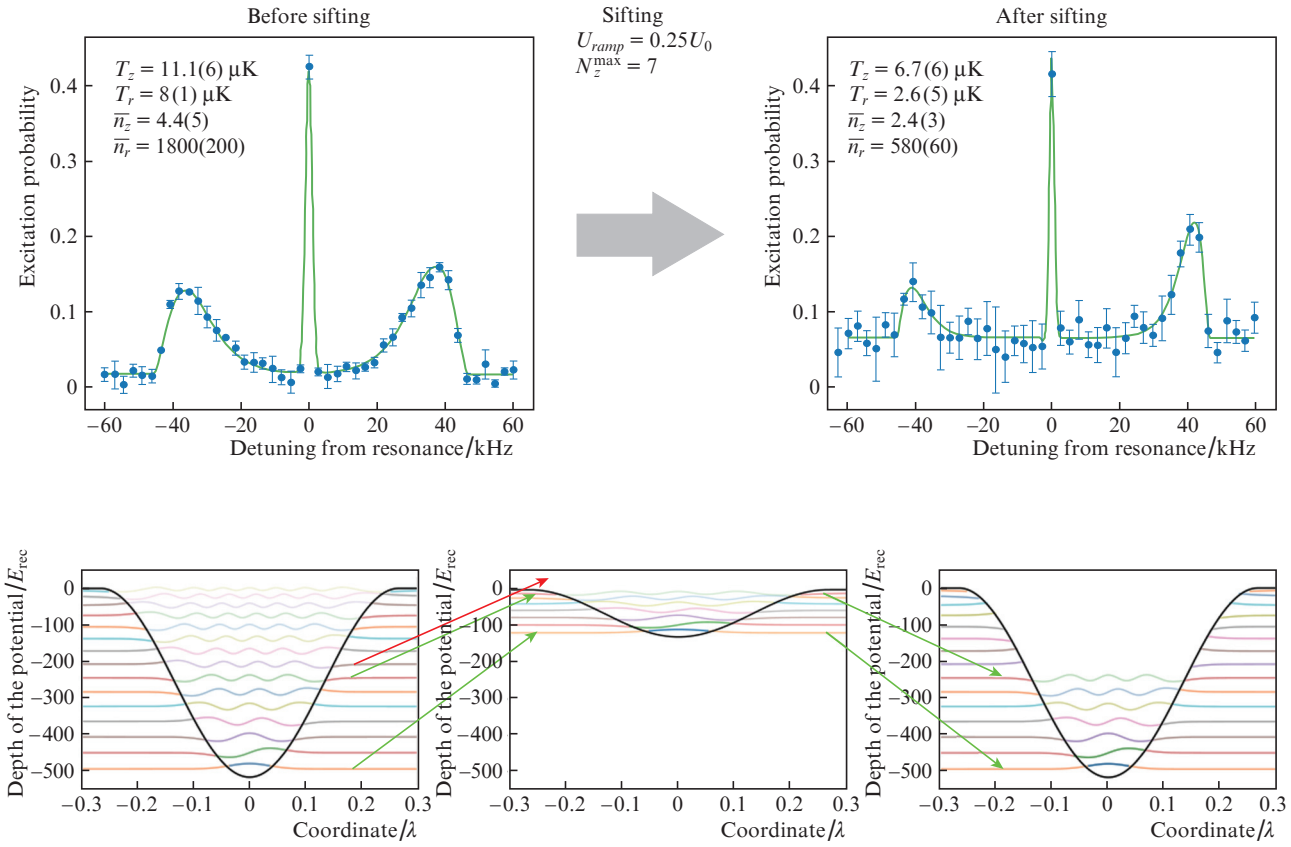

Figure 5. (Colour online) Sifting of atoms in an optical lattice via a temporary reduction in the depth of the confining potential from $516E_{rec}$ to $129E_{rec}$. Upper panels: experimentally measured vibrational sideband spectra before (left panel) and after (right panel) sifting (circles) and fitting of the experimental data to relation (7) (solid lines), with characteristic distribution parameters indicated for each experiment. Lower panels: simulation results for levels and their populations in the optical lattice potential [spatial distribution of the potential along the axis (black lines)] and illustration of wave functions at the corresponding eigenenergies in units of the recoil energy (coloured lines: their brightness represents the population of the corresponding level). The eigenenergies and wave functions at the potential of an isolated antinode of the optical lattice with the corresponding depth were found numerically.

ments, which corresponds to a constant relative population of the central magnetic sublevel. Using relation (7) and the above spectra, we estimated the corresponding temperatures of atoms and the average number of filled vibrational sublevels. In calculating the distribution over vibrational levels after sifting, we used both a thermodynamic distribution of atoms and a 'truncated' distribution, in which atoms were not thermalised after sifting and the number of filled sublevels was determined by the minimum depth of the potential during sifting. At the sifting depth in question, a large number of levels turn out to be filled in both cases, and the only distinction is in the population of slightly filled upper states. They cannot be distinguished numerically, so a deeper sifting is needed, to a level below 10% of the initial potential. In all the cases under consideration, the average number of populated vibrational sublevels along both longitudinal and transverse coordinates was found to decrease.

It is also important to pay attention to the fact that the number of atoms is determined by the minimum depth of the potential during the sifting process. This allows one to obtain the same number of atoms at different final optical lattice powers, which significantly facilitates analysis of results of experiments in which it is necessary to vary the lattice power, e. g. experiments in which the magic wavelength is sought [17].

The minimum sifting depth in the experiment was of the order of 25% of the initial one, which corresponded to a 6-W power of the beam propagating in the forward direction (Fig. 4), which corresponds, according to calculations, to a factor of 2 decrease in the number of bound states in the lattice potential. The minimum sifting depth in the experiment was determined by specific features of enhancement cavity stabilisation: with decreasing optical power, the amplitude of the error signal drops, which makes it impossible to stabilise the cavity length without changing parameters of the PID controller. To resolve this issue, a specialised scheme is being developed, with the possibility of automatically correcting parameters of the PID controller during experiments. According to estimates, 'cooling' to the vibrational ground state requires that the potential be ramped down to a level of one hundredth of the maximum potential considered in this study. This will lead to a loss of about 83% of the trapped atoms, without however preventing measurements. To deplete the levels with $n_z > 1$ (Fig. 2a), the sifting depth should be 2% of the initial one.

6. Conclusions

Analysis of interaction of thulium atoms with the optical lattice field has shown that it is necessary to cool the atoms to their vibrational ground state. This condition should be met for assessing higher order polarisabilities and characterising shifts and uncertainties in evaluation of the clock transition frequency at a level of 10^{-18}. In this work, we have demonstrated experimental applicability of the sifting method for removing atoms from high vibrational levels without changing the distribution of the atoms over magnetic sublevels. At initial parameters, of the order of 17% of the trapped atoms are in the vibrational ground state after optical pumping, which is sufficient for clock transition spectroscopy. This method makes it possible to reduce the number of populated vibrational levels to unity at a rather large decrease in the depth of the confining potential. For this purpose, however, a specialised enhancement cavity stabilisation scheme is needed, capable of operating in a wide range of input optical powers. For a more detailed analysis of the distribution of atoms over vibrational sublevels, we plan to use the dependence of the characteristic time of Rabi oscillation decoherence on the nature of the distribution.

Acknowledgements. This work was supported by the Russian Science Foundation (Grant No. 21-72-10108).

References

1. Hinkley N., Sherman A., Phillips N.B., Schioppo M., Lemke N.D., Beloy K., Pizzocaro M., Oates C.W., Ludlow A.D. *Science*, **341**, 1215 (2013).
2. Brewer S.M., Chen J.S., Hankin A.M., Clements E.R., Chou C.W., Wineland D.J., Hume D.B., Leibrandt D.R. *Phys. Rev. Lett.*, **123**, 033201 (2019).
3. Dörscher S., Huntemann N., Schwarz R., Lange R., Benkler E., Lipphardt B., Sterr U., Peik E., Lisdat C. *Metrologia*, **58**, 015005 (2021).
4. Bothwell T., Kedar D., Oelker E., Robinson J.M., Bromley S.L., Tew W.L., Ye J., Kennedy C.J. *Metrologia*, **56**, 065004 (2019).
5. Vishnyakova G.A., Golovizin A.A., Kalganova E.S., Sorokin V.N., Sukachev D.D., Khabarova K.Yu., Kolachevsky N.N. *Phys. Usp.*, **59**, 168 (2016) [*Usp. Fiz. Nauk.*, **186** (2), 176 (2016)].
6. Bergquist J.C., Itano W.M., Wineland D.J. *Phys. Rev. A*, **36**, 428 (1987).
7. Katori H. *Freq. Stand. Metrol.*, **1**, 323 (2002).
8. Belotelov G.S., Ovsiannikov V.D., Sutyrin D.V., Gribov A.Y., Berdasov O.I., Pal'chikov V.G., Slyusarev S.N., Blinov I.Y. *2020 Laser Phys.*, **30**, 045501 (2020).
9. Brown R.C., Phillips N.B., Beloy K., McGrew W.F., Schioppo M., Fasano R.J., Milani G., Zhang X., Hinkley N., Leopardi H., Yoon T.H., Nicolodi D., Fortier T.M., Ludlow A.D. *Phys. Rev. Lett.*, **119**, 253001 (2017).
10. Semenko A.V., Belotelov G.S., Sutyrin D.V., Slyusarev S.N., Yudin V.I., Taichenachev A.V., Ovsiannikov V.D., Pal'chikov V.G. *Quantum Electron.*, **51** (6), 484 (2021) [*Kvantovaya Elektron.*, **51** (6), 484 (2021)].
11. Fedorova E.S., Tregubov D.O., Golovizin A.A., Mishin D.A., Provorchenko D.I., Khabarova K.Yu., Sorokin V.N., Kolachevsky N.N. *Quantum Electron.*, **50** (3), 220 (2020) [*Kvantovaya Elektron.*, **50** (3), 220 (2020)].
12. Ushijima I., Takamoto M., Katori H. *Phys. Rev. Lett.*, **121**, 263202 (2018).
13. Hamann S.E., Haycock D.L., Klose G., Pax P.H., Deutsch I.H., Jessen P.S. *Phys. Rev. Lett.*, **80**, 4149 (1998).
14. Provorchenko D.I., Tregubov D.O., Mishin D.A., Golovizin A.A., Fedorova E.S., Khabarova K.Yu., Sorokin V.N., Kolachevsky N.N. *Quantum Electron.*, **51** (6), 479 (2021) [*Kvantovaya Elektron.*, **51** (6), 479 (2021)].
15. Golovizin A.A., Tregubov D.O., Fedorova E.S., Mishin D.A., Provorchenko D.I., Khabarova K.Y., Sorokin V.N., Kolachevsky N.N. *Nat. Commun.*, **12**, 5171 (2021).
16. Fedorova E., Golovizin A., Tregubov D., Mishin D., Provorchenko D., Sorokin V., Khabarova K., Kolachevsky N. *Phys. Rev. A*, **102**, 063114 (2020).
17. Golovizin A., Fedorova E., Tregubov D., Sukachev D., Khabarova K., Sorokin V., Kolachevsky N. *Nat. Commun.*, **10**, 1724 (2019).
18. Golovizin A., Bushmakin V., Fedorov S., Fedorova E., Tregubov D., Sukachev D., Khabarova K., Sorokin V., Kolachevsky N. *J. Russ. Laser Res.*, **40**, 540 (2019).
19. Tregubov D.O., Golovizin A.A., Fedorova E.S., Mishin D.A., Provorchenko D.I., Khabarova K.Yu., Sorokin V.N., Kolachevsky N.N. *Quantum Electron.*, **50** (6), 566 (2020) [*Kvantovaya Elektron.*, **50** (6), 566 (2020)].
20. Blatt S., Thomsen J.W., Campbell G.K., Ludlow A.D., Swallows M.D., Martin M.J., Boyd M.M., Ye J. *Phys. Rev. A*, **80**, 052703 (2009).
21. Katori H., Takamoto M., Pal'chikov V.G., Ovsiannikov V.D. *Phys. Rev. Lett.*, **91**, 173005 (2003).

22. Beloy K., Mcgrew W.F., Zhang X., Nicolodi D., Fasano R.J., Hassan Y.S., Brown R.C., Ludlow A.D. *Phys. Rev. A*, **101**, 053416 (2020).
23. Lee S.K., Lee H.W. *Phys. Rev. A*, **74**, 063817 (2006).
24. Sukachev D., Fedorov S., Tolstikhina I., Tregubov D., Kalganova E., Vishnyakova G., Golovizin A., Kolachevsky N., Khabarova K., Sorokin V. *Phys. Rev. A*, **94**, 022512 (2016).
25. Golovizin A.A., Kalganova E.S., Sukachev D.D., Vishnyakova G.A., Semerikov I.A., Soshenko V.V., Tregubov D.O., Akimov A.V., Kolachevsky N.N., Khabarova K.Yu., Sorokin V.N. *Quantum Electron.*, **45** (5), 482 (2015) [*Kvantovaya Elektron.*, **45** (5), 482 (2015)].
26. Kalganova E.S., Golovizin A.A., Shevnin D.O., Tregubov D.O., Khabarova K.Yu., Sorokin V.N., Kolachevsky N.N. *Quantum Electron.*, **48** (5), 415 (2018) [*Kvantovaya Elektron.*, **48** (5), 415 (2018)].